The Astrophysical Journal, 1001:16 (13pp), 2026 April 10 https://doi.org/10.3847/1538-4357/ae4eda

Understanding the Formation and Eruption of Sigmoidal Structure through Data-driven Modeling of Magnetic Evolution in Solar Active Region 13500

P. Vemareddy[1], S. Nair[1,2], and S. Gosain[3]
[1] Indian Institute of Astrophysics, II Block, Koramangala, Bengaluru-560 034, India; vemareddy@iiap.res.in, sreenair1202@gmail.com
[2] National Institute of Technology, Warangal-506 004, India
[3] National Solar Observatory, 3665 Discovery Drive, Boulder, 80303 CO, USA; sgosain@nso.edu
Received 2025 November 17; revised 2026 March 6; accepted 2026 March 7; published 2026 April 2

Abstract

We investigate the magnetic origin of the coronal mass ejection that occurred on 2023 November 28 at 19:50 UT from NOAA Active Region 13500 located near the solar disk center. The eruption was associated with an S-shaped sigmoidal structure formed by the inner active region (AR) polarities along a sheared polarity inversion line, while the outer polarities evolved through proper motions. During 2023 November 26–28, the AR exhibited a decrease in net magnetic flux, while progressively injecting magnetic helicity and energy into the corona toward the eruption onset, highlighting the key role of helicity injection in triggering eruptions. To simulate this magnetic evolution, we employed a data-driven magnetofrictional (MF) simulation starting 2.8 days prior to the eruption. The energy input for the model was constrained using the observed energy injection through an ad hoc parameter. The initial potential-field configuration gradually evolved into a sheared arcade and eventually developed into a twisted flux rope (FR) over the observed timescale. Proxy emission maps based on electric currents show remarkable morphological agreement between the simulated and observed sigmoidal structures. The average FR core twist increasingly builds up, leading the FR to initiate a slow-rise motion of the FR top from 50 Mm until its eruption onset at 80 Mm. Importantly, the ratio of the current-carrying to total relative helicity increased from 0.13 at the FR formation to 0.30 at eruption, when the FR core entered the torus-unstable regime, suggesting an association between torus instability and the threshold helicity ratio. These results demonstrate that data-driven MF simulations can successfully reproduce the evolving coronal magnetic configuration and may provide a robust tool for assessing the eruptive potential of ARs, particularly the helicity ratio.

Unified Astronomy Thesaurus concepts: Solar active regions (1974); Solar coronal mass ejections (310); Magnetohydrodynamical simulations (1966); Solar active region filaments (1977); Solar active region magnetic fields (1975); Solar evolution (1492)

1. Introduction

Solar flares and coronal mass ejections (CMEs) are massive explosive phenomena representing significant solar activity that varies with the 11 yr sunspot cycle. During these events, vast amounts of magnetized plasma are expelled from localized regions in the solar atmosphere into space, accompanied by bursts of electromagnetic radiation, including X-rays and ultraviolet light. These phenomena are fundamental drivers of space weather, affecting Earth's magnetosphere and technological systems (M. Temmer 2021; J. Zhang et al. 2021). The energy powering these events originates from concentrated magnetic field regions, such as active regions (ARs), though the exact mechanisms of energy storage and eruption onset are still debated (e.g., T. G. Forbes 2000; L. M. Green et al. 2018).

The study of magnetic field evolution is central to understanding how magnetic energy is stored and released over a range of time scales. Several observational studies have highlighted that the magnetic field evolution comprises three characteristic types of mechanisms that contribute dominantly to the buildup of free magnetic energy in the solar atmosphere. These include: (1) the emergence or cancellation of magnetic flux (H. Zhang 1995; K. D. Leka et al. 1996; P. F. Chen & K. Shibata 2000; A. C. Sterling et al. 2010); (2) shearing motions between opposite-polarity magnetic fields (A. Ambastha et al. 1993; P. Démoulin et al. 2002; P. Vemareddy 2017; G. Chintzoglou et al. 2019); and (3) the rotation of sunspots (e.g., D. S. Brown et al. 2003; L. Tian & D. Alexander 2006; P. Vemareddy et al. 2012a, 2016). While the evolution of magnetic fields results in energy storage, simultaneous observations reveal distinct pre-eruptive coronal structures, such as X-ray sigmoids, Hα filaments/prominences, and EUV hot channels. These features are interpreted as twisted magnetic fields formed due to stresses at the foot points of magnetic field lines. The nonpotentiality of these twisted fields is quantified using a variety of measures, such as electric currents, magnetic free energy, and magnetic helicity, etc. (e.g., P. Vemareddy et al. 2012a; E. Pariat et al. 2017; F. P. Zuccarello et al. 2018), which, in turn, serves to determine the ability of an AR to produce eruptions. Studying magnetic field evolution makes it essential to understand the mechanisms of twisted flux formation, to identify the eruption's stage and trigger, and to estimate the amount of stored magnetic energy and other nonpotential parameters.

Studying magnetic field evolution requires observations of the magnetic fields in the 3D corona. Since routine coronal magnetic field measurements are not available, extrapolation techniques have been developed to construct 3D magnetic fields based on photospheric magnetic field measurements (C. J. Schrijver et al. 2008; T. Wiegelmann & T. Sakurai 2012). Typically, these models assume that the coronal magnetic field is force-free, meaning there is a zero Lorentz

force. This assumption arises from the low-β plasma conditions and the large Alfvén speed relative to the photospheric flow speed. Consequently, the evolution of the coronal magnetic field is described as a quasi-static process by a sequence of successive force-free equilibria in response to changes in the surface magnetic field (e.g., J. J. Aly 1990; P. Vemareddy & T. Wiegelmann 2014). Additionally, the magnetofrictional (MF) method is another technique used to construct force-free coronal magnetic fields, based on a simplified induction equation (W. H. Yang et al. 1986). Recently, time-dependent, data-driven MF models, with a provision to inject sufficient energy and helicity from the bottom boundary of the computational domain, have been developed to study the long-term evolution of ARs (M. C. M. Cheung & M. L. DeRosa 2012; J. Pomoell et al. 2019; P. Vemareddy 2024) over several days. Compared to static extrapolation techniques, these models have the advantage of capturing dynamic evolution while retaining memory from previous equilibrium stages.

The objective of this study is to simulate the magnetic evolution of NOAA Active Region 13500 using a data-driven MF method. This AR was in its decay phase at the time of interest, exhibiting a decreasing magnetic flux content, and produced a fast CME associated with a sigmoidal eruption. In particular, this work aims to capture both the formation and eruption of the sigmoid structure by self-consistently modeling the magnetic field evolution with photospheric vector magnetic field observations. Previous data-driven MF simulations of NOAA Active Region 11149 have effectively reproduced the formation of twisted flux along the main polarity inversion line (PIL) with an unprecedented morphological agreement with observations (P. Vemareddy 2024), highlighting the promising capabilities of these models. With such a robust modeling tool, one can assess the variety of nonpotential parameters, especially the ratio of the nonpotential magnetic helicity and the total relative magnetic helicity (E. Pariat et al. 2017; F. P. Zuccarello et al. 2018), for their ability to predict the eruptive potential of an AR. The zero-β simulations of F. P. Zuccarello et al. (2018) suggested that eruptive ARs possess a helicity ratio of approximately 0.29, which is coincident with the onset of torus instability; however, this association requires verification in several AR cases for the general validity of the helicity threshold. The manuscript is organized as follows. Section 2 presents the observations of the AR and its magnetic evolution leading to the CME. Section 3 provides the simulation results and their comparison with the observations, along with the characteristic nonpotential parameters describing the eruptive potential of the AR. A summary with a brief discussion is given in Section 4.

2. Observations and Analysis

We studied the magnetic origins of the CME that occurred on 2023 November 28 at 19:50 UT. This CME was identified as the solar source of an intense geomagnetic storm on 2023 December 1, which began at 01:00 UT and peaked at −105 nT around 12:00 UT the same day.

2.1. The CME and Its Source Region

Observations of the source region were obtained using instruments on board the Solar Dynamics Observatory (SDO). The Atmospheric Imaging Assembly (AIA; J. R. Lemen et al. 2012) continuously monitors the full solar disk at seven EUV wavelengths, capturing dynamical processes from the chromosphere to the corona with a 12 s cadence and 0.″6 per pixel resolution. Magnetic field measurements at the photosphere were obtained using the Helioseismic and Magnetic Imager (HMI; J. Schou et al. 2012), which has a pixel resolution of 0.″5 and a cadence of 12 minutes. White-light observations of the extended corona up to 32 $R_\odot$ are obtained from the Large Angle and Spectrometric Coronagraph (LASCO) instrument on board the Solar and Heliospheric Observatory. Figure 1(a) displays the full-disk image of the Sun in the AIA 304 Å wave band, showing AR 13500 located near the disk center ($S20^oW04^o$) on November 28. The coronal emission is structured, featuring an S-shaped sigmoidal morphology (Figures 1(a), (d), and (e)). The onset of the eruption (CME launch) occurred at around 19:15 UT, as seen by AIA 193 Å running-difference images, displayed in Figure 1(b). The CME started emerging in the LASCO/C2 field of view (FOV) from 20:12 UT as a full-halo event, which can be noticed in Figure 1(c) of the running-difference LASCO/C2 image. This eruption was associated with an M9.8 solar flare that began at 19:35 UT and peaked at 19:50 UT (Figure 1(f)). The CME's linear speed, as measured in the LASCO FOV, was 741 km s^{-1}. The travel time of this CME to Earth was ≈53 hr. In the subsequent sections, we analyze the magnetic evolution of the AR that led to the formation and eruption of the sigmoidal structure, and we employ data-driven simulations to gain insights into the mechanisms behind the eruption.

2.2. Magnetic Evolution of the AR

Figure 2 displays observations of the vector magnetic field in the photosphere of the AR during different stages of its evolution. The overall polarity distribution of the AR follows Hale's polarity law for solar cycle 24, with the leading polarity being negative and the following polarity positive in the southern hemisphere. Notably, the AR contains inner opposite-polarity regions, labeled "N2" and "P2," as well as outer polarity regions of the same orientation, labeled "N1" and "P1," as observed on November 26. The inner pair creates a PIL, which generates a sheared magnetic field as the regions move slowly in opposite directions over time. Meanwhile, the N1 region, initially close to the N2 region on 2023 November 26, experiences proper motion and becomes detached by the end of 2023 November 28.

Importantly, the sizes of the polarities decrease over the 2 days of evolution, which is reflected in the decreasing net magnetic flux shown in Figure 3(a). The underlying flux motions are key to the injection of helicity and magnetic energy into the AR (P. Vemareddy et al. 2012b; P. Vemareddy 2015). Due to these slow footpoint motions, the magnetic fields are stressed and develop largely field-aligned electric currents, which can be seen in the evolution of the net electric current shown in Figure 3(b) in each polarity (I_N and I_S, respectively) toward the eruption time. As a result, the net average force-free twist parameter α_{av} (shown in the same panel) also exhibits an increasing trend.

Using a time sequence of the vector magnetic fields, we first derive the vector velocity, $\boldsymbol{V}$, of the flux motions using the DAVE4VM (P. W. Schuck 2008) technique, then compute the helicity flux injection from the photospheric surface

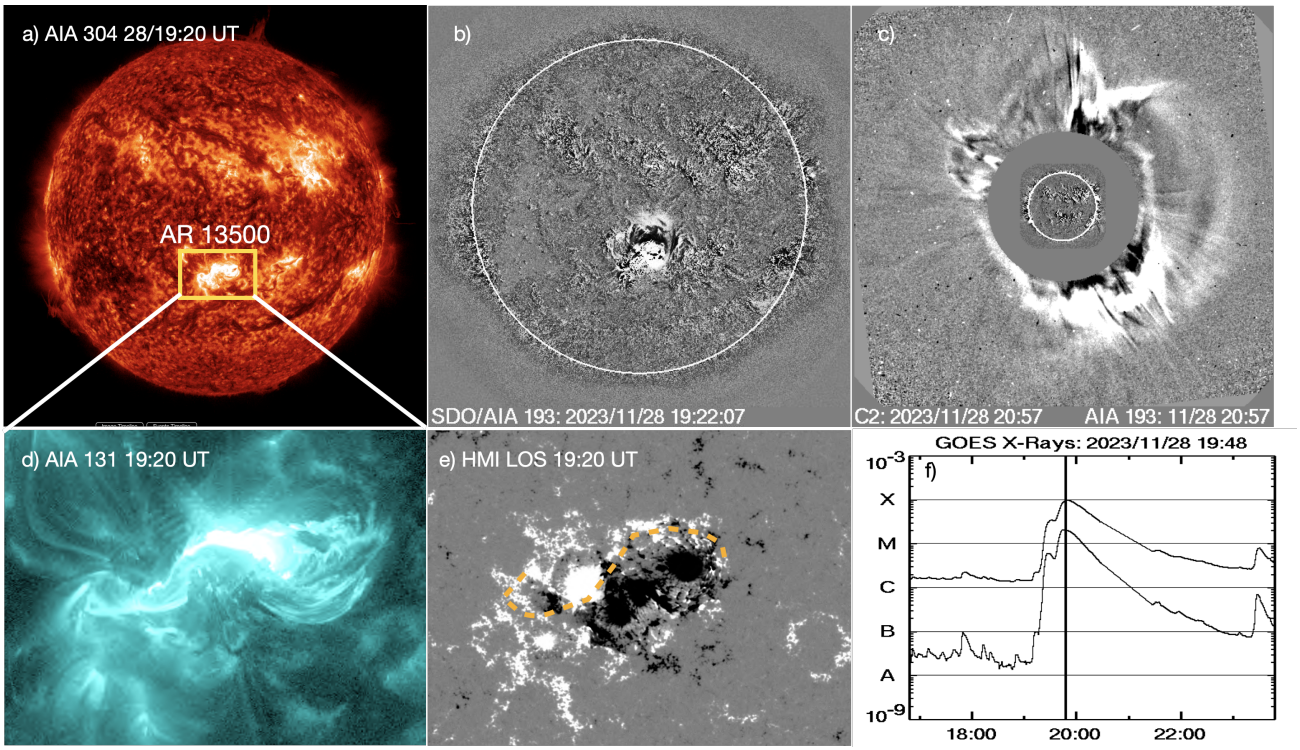

Figure 1. Multiobservation scenario of the CME eruption from AR 13500 on 2023 November 28. (a) Full-disk image of the Sun in AIA 304 Å showing the AR location (yellow rectangular box). (b) Running-difference image in AIA 193 Å, indicating the onset of the eruption from AR 13500. (c) LASCO/C2 difference image showing the halo/CME emerging from the Sun. (d) AIA 131 Å image of AR 13500 with an S-shaped sigmoid. (e) HMI magnetogram displaying the magnetic field distribution in the AR—for comparison, the trace of the sigmoid is overlaid (yellow dashed curve). (f) GOES X-ray flux light curve referring to the M9.8 flare starting from 28T19:35 UT.

(M. A. Berger & G. B. Field 1984) as

$$\left.\frac{dH}{dt}\right|_S = 2\int_S (\boldsymbol{A}_p \cdot \boldsymbol{B}_t) V_n \, dS - 2\int_S (\boldsymbol{A}_p \cdot \boldsymbol{V}_t) B_n \, dS. \quad (1)$$

As shown in Figure 3(c), the dH/dt increases predominantly with a positive sign from early on 2023 November 27 to the time of eruption, which is linked to the polarities in shearing motion. The dH/dt reaches around 3×10^{37} $\mathrm{Mx^2\,s^{-1}}$ toward the end of 2023 November 27, following a phase of increasing positive-sign helicity injection. Especially, the peak $dH/dt = 13 \times 10^{37}$ $\mathrm{Mx^2\,s^{-1}}$ occurs at 18:00 UT on 2023 November 28 (vertical dotted line), which is cotemporal with the onset time of the CME and the associated M9.8 flare. The leading N1 polarity exhibits a separating motion from 2023 November 27; the jump in the dH/dt at the time of eruption likely corresponds to the detaching of N1 from N2. By the time of eruption, the AR has accumulated a net helicity of around $5 \times 10^{42}\,Mx^2$, which is significant for an eruptive potential.

Since the helicity is proportional to the square of the net magnetic flux (M. A. Berger & G. B. Field 1984), we express an average amount of AR twist injection, by normalizing both dH/dt and H by the square of the magnetic flux, Φ^2 (Figure 3(d)). By the time of the CME onset, H/Φ^2 has reached a value of 0.04 turns. This quantity is limited to 0.02 turns in ARs that produce confined flares but has been found to be as high as 0.15 turns during 6 days of evolution in successively erupting ARs, as reported in P. Vemareddy (2017, 2019).

3. Simulating the Magnetic Evolution of the AR

We employ a data-driven MF model to simulate the magnetic evolution of the AR, as detailed in recent works (M. C. M. Cheung & M. L. DeRosa 2012; J. Pomoell et al. 2019; P. Vemareddy 2024). We implement this simulation model in the PENCIL code, with an additional special driver module to supply the observed magnetic fields at the bottom of the computational grid while the simulation advances in time (P. Vemareddy et al. 2024). The initial field is a potential field (PF), which is then driven by electric fields that are derived from time-varying photospheric vector magnetic field observations (G. H. Fisher et al. 2010). In order to inject sufficient helicity and energy into the coronal field, the electric field is additionally supplied with a noninductive contribution controlled by an ad hoc parameter, U.

Figure 4 plots the Poynting flux, dE/dt, derived from the direct magnetic field and velocity field (top panel) in comparison with that derived from the electric field being used as the driver field (bottom panel). Starting from 2023 November 26, the total magnetic energy, E, accumulated by the time of the eruption (28T19:12 UT; 67 hr of evolution) is 4×10^{32} erg, which is to be constrained in the simulation through the driver electric field. As shown in the plot, the electric field derived with an ad hoc parameter of $U = 150$ $\mathrm{m\,s^{-1}}$ better represents the energy injection scenario in the observations, which is being used to simulate the coronal field evolution.

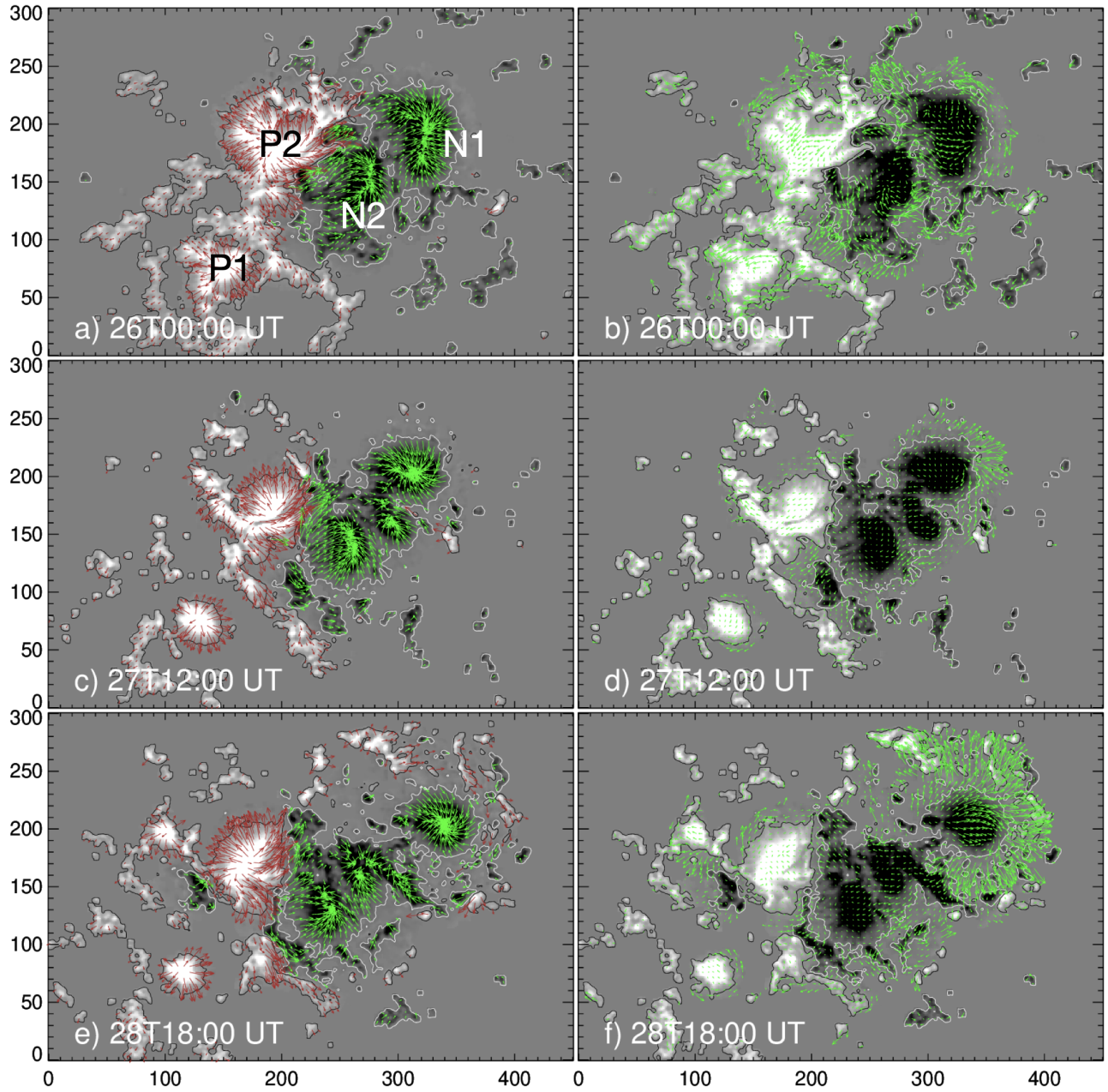

Figure 2. Left: HMI vector magnetograms of AR 13500 at different epochs of its evolution. Right: the derived velocity of the flux motions. Arrows referring to the horizontal field are overplotted on the vertical component of the magnetic field. Prominent polarities are labeled in panel (a). Notice that while N2 and P2 move antiparallel to one another, N1 separates from N2 with a proper motion. The axis units are in pixels of 0.″5 size.

In the first two columns of Figure 5, snapshots of the simulated magnetic field are displayed at different times. To visualize the twisted fields, we trace field lines at locations of strong electric currents in the lower part of the computational domain. The simulation begins with the PF constructed from the radial component of the vector magnetic field observations at 26T00:00 UT. The initial PF comprises an inner arcade along the PIL, which is enveloped by an outer arcade that connects the peripheral parts of opposite polarities. This configuration evolves slowly with the changing boundary conditions, still largely resembling a PF until about 25 hr into the simulation. This behavior is consistent with the energy being injected from the bottom boundary (see Figure 4). As the energy and helicity accumulate, further evolution transforms the inner arcade into a sheared arcade, which eventually develops into a highly twisted structure (i.e., into flux rope or FR) resembling a sigmoid, as observed in the snapshot at 50 hr of the simulation, corresponding to the end of 2023 November 27. In the third column of Figure 5, we present the total current ($|\boldsymbol{J}|$) distribution in a vertical cross section that is placed across this twisted structure (FR). These panels illustrate the formation and slow ascent of the FR over the 3 days of the simulation. We observe that the top of the FR reaches a height of around 50 Mm by 50 hr and extends to almost 80 Mm by 68 hr (the observed eruption time), which is a part of quasi-static evolution. With the driving boundary conditions, the FR builds by developing strong electric currents, and the Lorentz force overcomes the tension of the overlying field. As a result, the

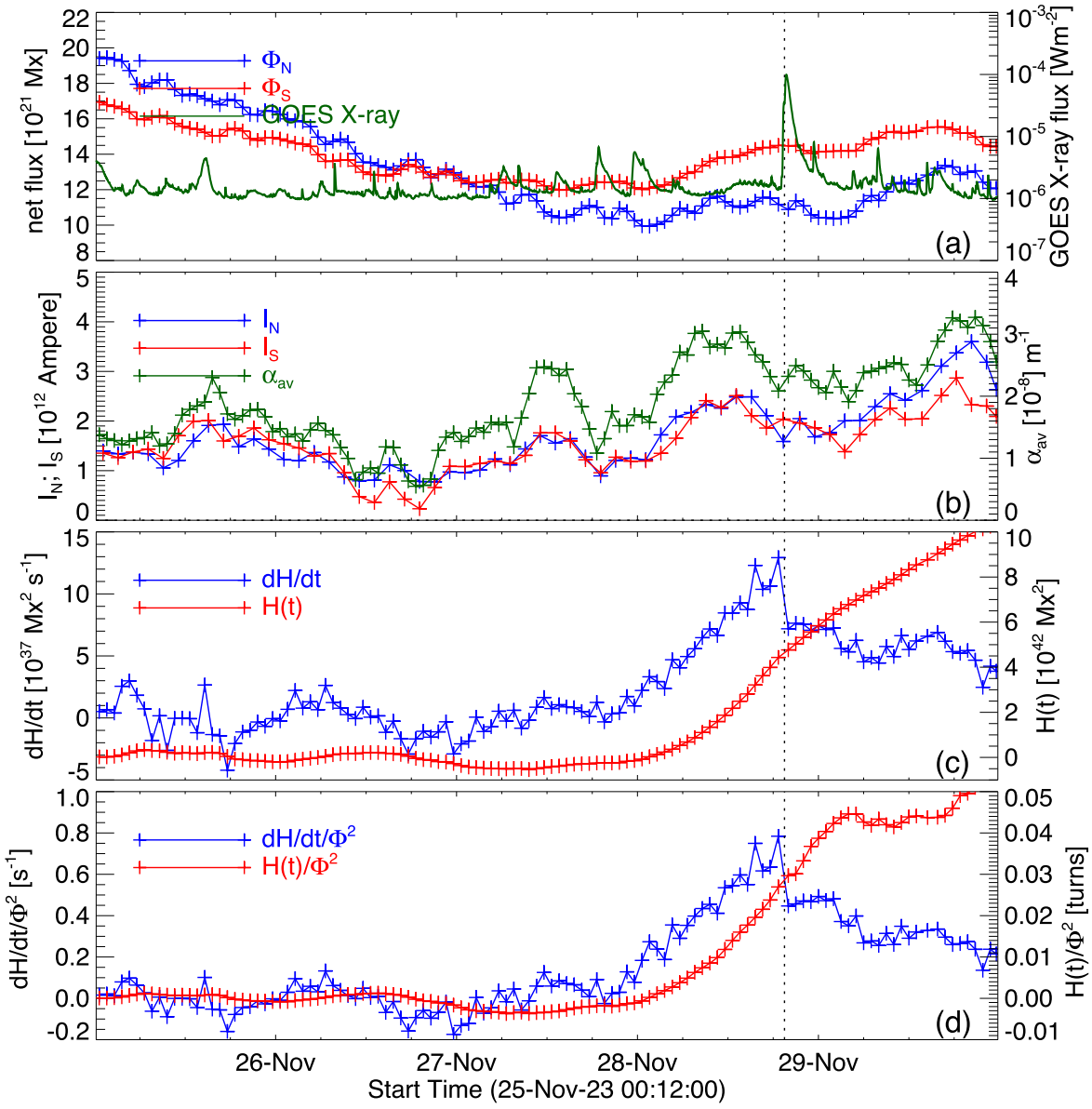

Figure 3. Time evolution of nonpotential parameters in AR 13500. (a) The net magnetic flux showing a decreasing flux content as it evolves over time with interacting magnetic polarities. The GOES flux is also shown with the *y*-axis scale on the right. (b) The net vertical current in each polarity flux region, along with the average twist parameter (α_{av}). (c) The helicity injection rate (dH/dt, blue, *y*-axis on the left) and accumulated helicity $H(t)$ (red, *y*-axis on the right)—as marked by the vertical dotted line, the peak dH/dt is cotemporal with the CME eruption and the M9.8 flare. (d) The helicity flux normalized with the square of the magnetic flux.

FR experiences an upward slow-rise motion, as seen in this quasi-static phase of evolution. Observations indicate that preeruptive structures, such as prominences and EUV hot channels, are found at similar heights in the corona (e.g., J. Zhang et al. 2012; P. Vemareddy et al. 2022).

In Figure 6, we compare the simulated magnetic structure with the coronal observations at 45 hr, when the FR has formed. We note, at this point, that the transition from a sheared arcade to an (initially weakly twisted) FR is a gradual process, so it cannot be associated with a single point in time (e.g., S. Patsourakos et al. 2020). However, visual inspection of the field lines and the twist maps described below suggests that a well-developed FR is already present at this time. The comparison is done by generating a proxy emission map, which is obtained from integrating along the line of sight (here, in a top-down view) the average value of the square of the total current density, J^2, over magnetic field lines (see the details in M. C. M. Cheung & M. L. DeRosa 2012). As can be seen, the FR is cospatial with the sigmoidal feature in the proxy emission map. This sigmoidal feature has a remarkable morphological similarity with the one observed in the AIA 304Å image and the Hα image from the Kodaikanal Solar Observatory (KSO), especially regarding the orientation and curvature of its lobes. This indicates that our simulation successfully captures important characteristics of the coronal magnetic field in the AR.

To illustrate the slow ascent of the FR mentioned above, the proxy emission is extracted along a slice plane that captures the cross section of the FR, as depicted in Figures 7(a)–(c). The field-line twist (T_w) is also computed in the same plane

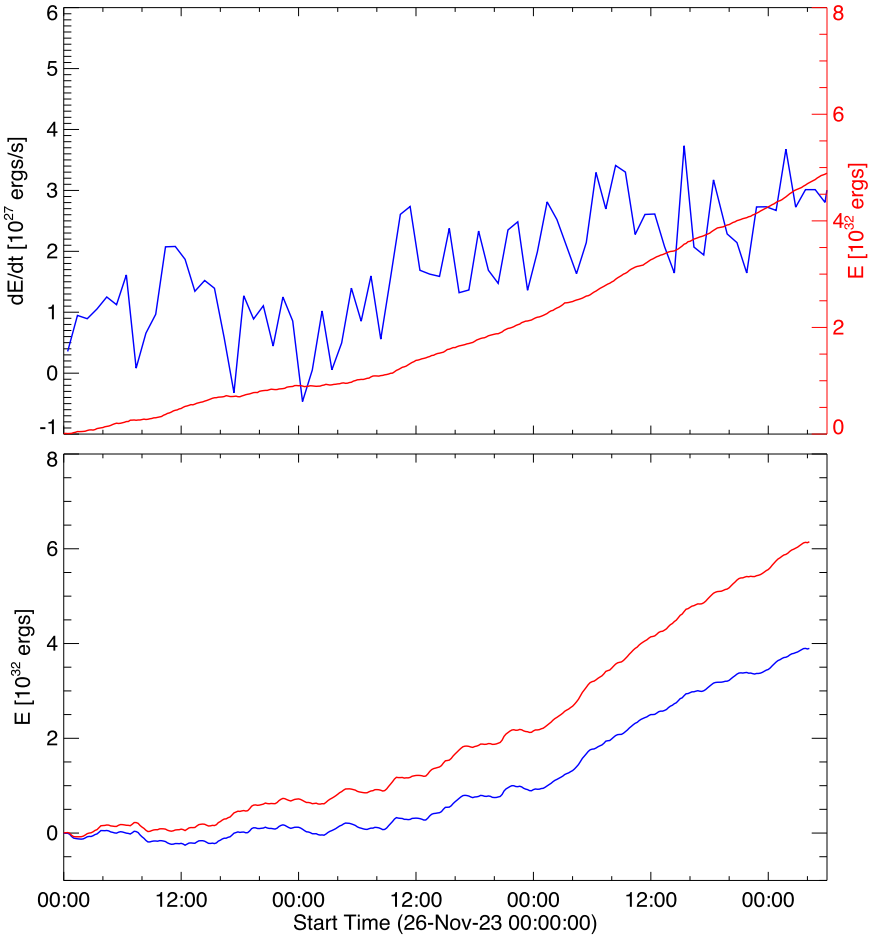

Figure 4. Constraining the energy injection for MF simulations from vector field observations. Top: computed Poynting flux (dE/dt) and its accumulated quantity from the observed magnetic field at the photospheric surface. Bottom: accumulated Poynting flux from the electric fields derived with $U = 120$ m s^{-1} (blue) and $U = 150$ m s^{-1} (red).

with the expression (M. A. Berger & C. Prior 2006; R. Liu et al. 2016)

$$T_w = \int_L \frac{\mu_0 \boldsymbol{J}_{\parallel}}{4\pi B}\, dl = \int_L \frac{\nabla \times \boldsymbol{B} \cdot \boldsymbol{B}}{4\pi B^2}\, dl, \quad (2)$$

as shown in Figures 7(d)–(f). These panels clearly illustrate that the FR rises gradually, with its top reaching a height of approximately 80 Mm by 65 hr. It is noteworthy that the maximum twist within the FR core (enclosed by the yellow oval) is about 3.2 turns, while the average twist increases from 1.28 turns at 55 hr to 1.43 turns at 65 hr, indicating a development of the helical kink instability, according to T. Török et al. (2004), which could have initiated the onset of the eruption. Note that the core of the FR is around 40 Mm.

To better assess the evolution of the slow FR rise, we prepared a stack of vertical slits from each plane cut of the FR. For clarity, from Figure 7, a slit is extracted at around 80 Mm along the x-direction, from which a twist map is produced and presented in Figure 8. The red color is a positive twist of the FR; the more intense red corresponds to the core. The FR's gradual ascent becomes evident after its formation at around 45 hr, revealing a slow-rise motion as part of its further buildup and quasi-static evolution. By 65 hr, the FR (top, the point by the arrow) reaches a height of 80 Mm, and it rises further until the end of the simulation, at 96 hr. Note that the driver is switched off at 70 hr, just after the observed eruption at 67 hr. The rise motion thereafter, while slow, mimics the FR eruption. It is important to mention that a transition from the slow-rise motion until 67 hr to the later time is not present, as we usually observe during the initiation of the eruption (N. Vasantharaju et al. 2018), which is a drawback of MF simulations, as the velocity is controlled by the constant frictional parameters.

Figure 9 presents the time evolution of the computed relative magnetic helicity (H) and the magnetic energy (E) of the simulated magnetic field. The volume helicity (H) steadily accumulates from the start of the simulation, reaching a value of 10×10^{42} Mx^2 for the run using an electric field derived with $U = 120$ m s^{-1}. This value increases slightly to 14×10^{42} Mx^2 for the run with $U = 150$ m s^{-1}. Meanwhile, the total magnetic energy E decreases slightly from 10.5 to 8×10^{32} erg over 3 days of evolution. However, the free magnetic energy $E_f = E - E_p$ continuously increases, reaching 4×10^{32} erg in the case of the $U = 120$ m s^{-1} run. This observation can be explained by the fact that the AR is in a decay phase, resulting in a net

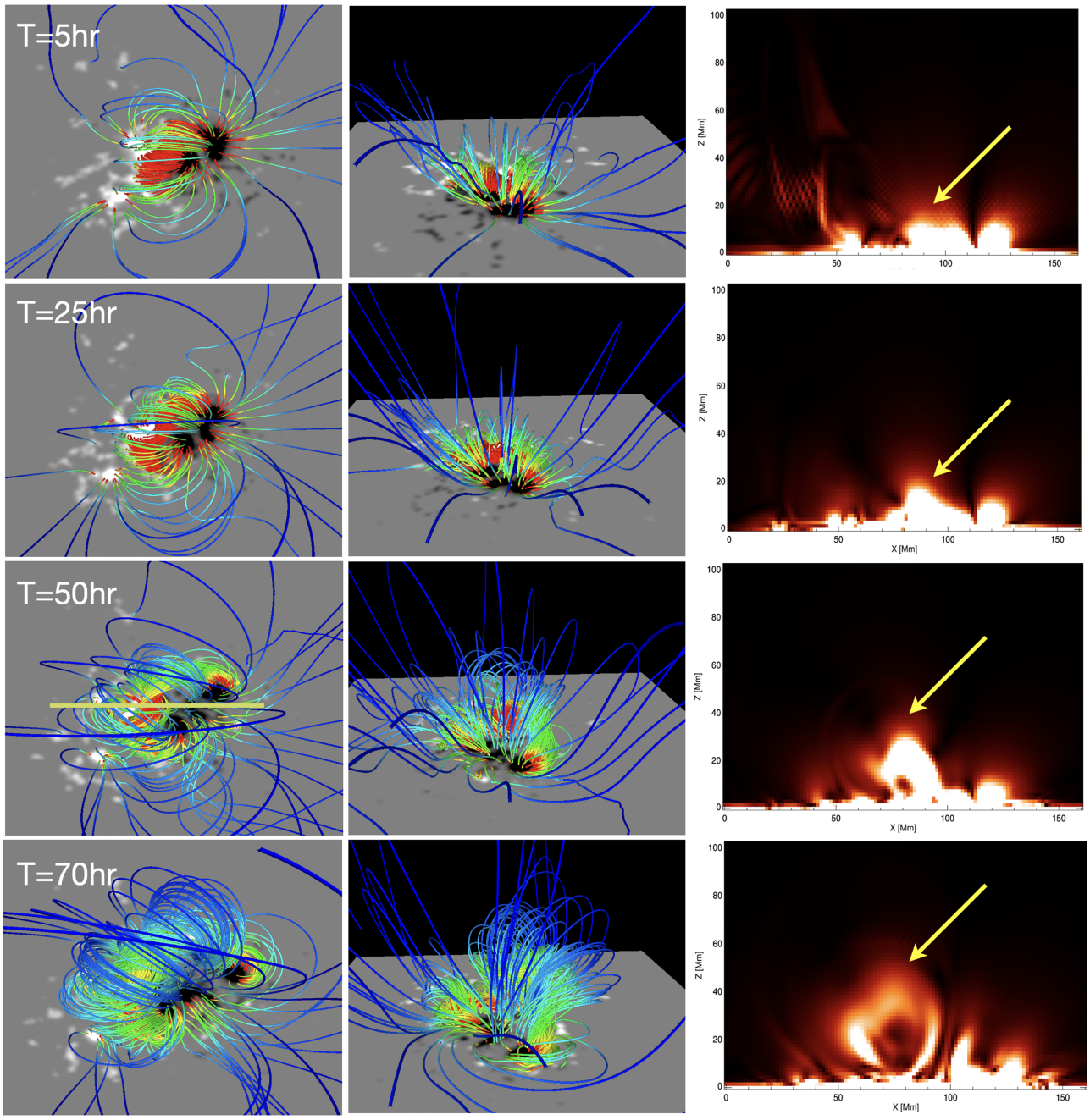

Figure 5. The evolution of the AR magnetic structure at different epochs of the simulation. First column: top view. Second column: perspective view. Third column: total current in the vertical cross section placed across the sigmoid. The magnetic field lines are colored by their field strengths, and the background image is the normal magnetic field Bz at the bottom of the computational domain ($z = 0$). The simulation captures the formation of the twisted FR by 50 hr along the PIL and its slow-rise motion later. The arrow points to twisted flux that is being formed and rises progressively.

decrease in magnetic energy during this time period. This example highlights that the total magnetic energy E is not a reliable indicator of the eruptive potential of an AR. Instead, the free magnetic energy E_f, which is associated with the nonpotential field, plays a crucial role and varies under different circumstances. At the time of the observed eruption, the fractional free energy (E_f/E) is 51% for the $U = 120\,\mathrm{m\,s^{-1}}$ run and 57% for the $U = 150\,\mathrm{m\,s^{-1}}$ run. According to previous studies (J. Pomoell et al. 2019; P. Vemareddy 2024), the latter run appears to have a higher potential for the eruption.

3.1. The H_J/H_V Ratio

According to M. A. Berger (2003), the relative magnetic helicity can be decomposed as $H_V = H_J + 2H_{PJ}$, with

$$H_J = \int_V (\boldsymbol{A} - \boldsymbol{A}_P) \cdot (\boldsymbol{B} - \boldsymbol{B}_p) dV$$

$$H_{PJ} = \int_V \boldsymbol{A}_p \cdot (\boldsymbol{B} - \boldsymbol{B}_p) dV.$$

Here, H_J is the magnetic helicity of the nonpotential or current-carrying component of the magnetic field $\boldsymbol{B}_J = \boldsymbol{B} - \boldsymbol{B}_p$, and

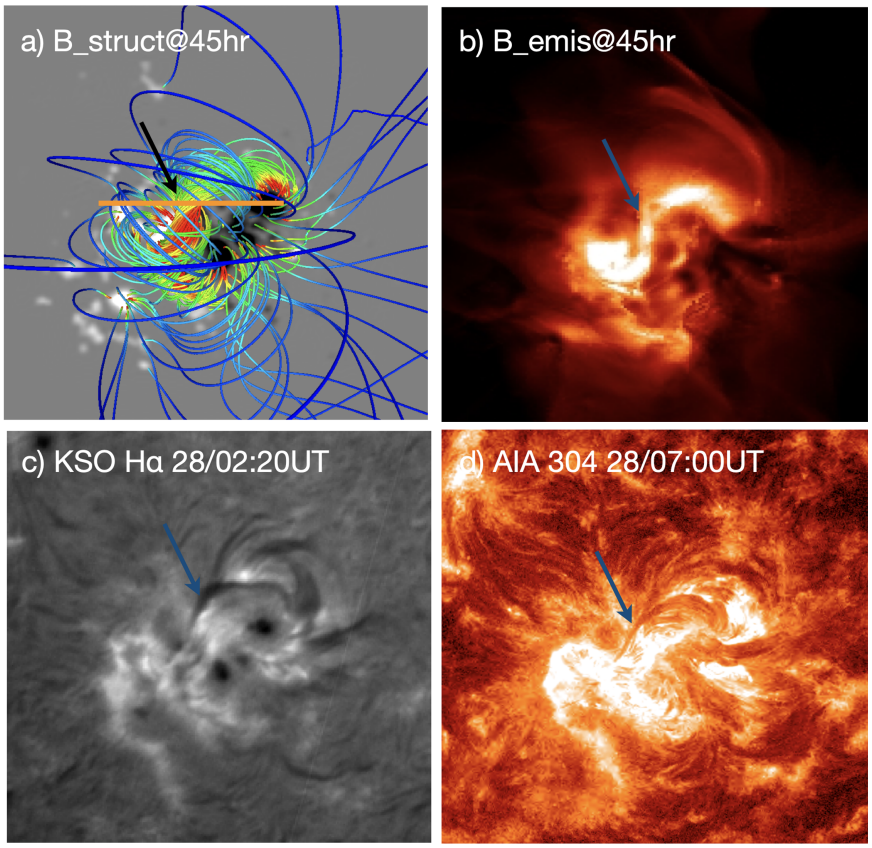

Figure 6. Comparison of the simulated magnetic structure with the coronal observations. (a) Rendered magnetic structure at 45 hr of the simulated field. (b) Proxy emission map of the simulated magnetic field. (c) AIA 304 Å image at 28T07:00 UT—note the striking morphological similarity of the simulated proxy emission with the AIA 304 Å image broadly reproducing the sigmoidal feature. (d) Hα image from KSO at 28T02:20 UT—the blue arrow points to the filament and its supporting magnetic structure.

H_{pJ} is the mutual helicity between $\boldsymbol{B}_p$ and $\boldsymbol{B}_J$. We evaluate these quantities in the entire simulation box, as shown in Figure 10(a). As the simulation progresses, both $H_{\rm PJ}$ and H_J accumulate steadily with pumping energy from the bottom boundary. At the time of the observed eruption, they reached $9.76 \times 10^{42}\,Mx^2$ and $4.12 \times 10^{42}\,Mx^2$, respectively. Since the bottom boundary's H_V is scaled by the square of the net average flux (Φ), we calculated H_V/Φ^2, as shown in Figure 10(b). Based on this, the average magnetic field twists at the recorded eruption time are 0.13 and 0.17 turns for the $U = 120$ and $150\,{\rm m\,s^{-1}}$ runs, respectively, which are comparable with the reported values of F. P. Zuccarello et al. (2018).

We also analyze the evolution of the ratio H_J/H_V, which has been shown to have a characteristic pattern that distinguishes eruptive from noneruptive ARs (E. Pariat et al. 2017; F. P. Zuccarello et al. 2018). This ratio exhibits an increasing trend over time, as illustrated in Figure 10(c). At the time of the eruption, H_J/H_V is observed to be 0.3 and 0.37 respectively, for the two runs. Previous studies have investigated the time series of nonlinear force-free extrapolations, indicating that the evolution of H_J/H_V differs between eruptive and noneruptive ARs where an AR is found to erupt when $H_J/H_V > 0.1$ (M. Gupta et al. 2021).

3.2. Evidence for Torus Instability

Additionally, using a series of line-tied MHD simulations, F. P. Zuccarello et al. (2018) showed that at the onset of the torus instability, the ratio $H_J/H_V \approx 0.29$, proposing it as a reliable proxy for identifying the instability threshold. This result, however, comes with an important caveat: the relative helicity H_V is not an additive quantity, and values of the helicity ratio computed over different volumes or with different boundary conditions can vary. In our study, both H_J and H_V are evaluated over the entire simulation domain, allowing the ratio to be interpreted meaningfully in the context of eruptive behavior in the AR. Since the simulated field is quasi-static, without fast eruptive signatures, we considered the observed time of eruption (67 hr) to assess the eruptive behavior of the magnetic structure.

Our results are consistent with these simulations, as we find $H_J/H_V \geqslant 0.3$ at the time of eruption. Comparable high values were also reported by L. M. Green et al. (2022), who analyzed AR 11158 using nonlinear force-free magnetic field extrapolations. While a condition of $H_J/H_V \geqslant 0.1$ has been suggested as sufficient for an AR to be susceptible to eruption, the onset of the torus instability appears to require larger values. This indicates that a threshold of $H_J/H_V \geqslant 0.3$ may be applicable for certain ARs, including the case examined here.

In our time-dependent MF simulation, the ratio reaches 0.1 once the twisted FR is well developed, after approximately 50 hr of evolution. Thereafter, it increases steadily, and by the time of the observed eruption, at around 65 hr, the FR apex reaches a height of about 80 Mm (with the FR core center located near 32 Mm; see Figure 7), signaling a strong eruptive potential. The subsequent rapid eruption phase is not captured

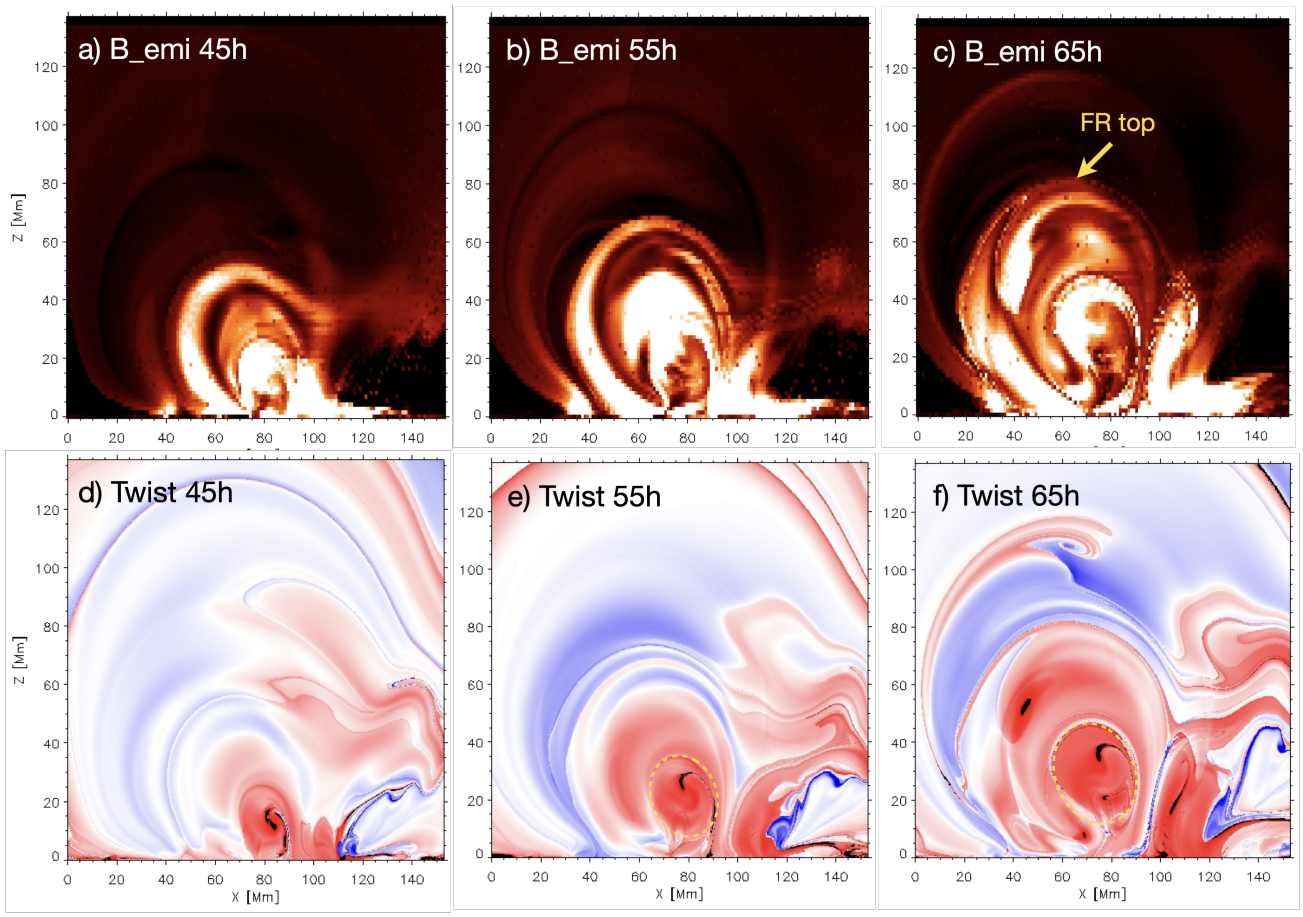

Figure 7. Buildup and onset of FR eruption. (a)–(c) Proxy emission in the vertical slice (the orange line in Figure 6(a)) at different epochs, showing the slow upward-moving FR with its top reaching 80 Mm by 65 hr. (d)–(f) Twist maps in the vertical slice: the red (blue) color indicates positive (negative) or right-handed (left-handed) twist scaled to 2 turns; the core of the FR is indicated with the yellow oval, within which the average field-line twist increases from 1.28 turns at 55 hr to 1.43 turns at 65 hr.

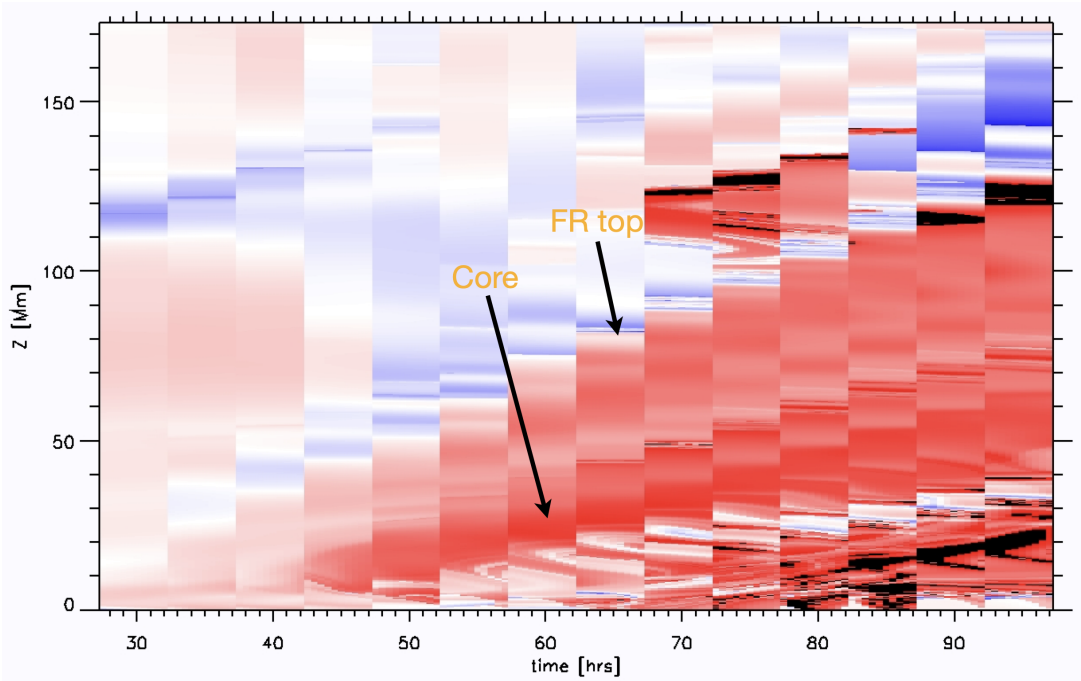

Figure 8. Spacetime map of the twist along the FR height, in a plane as shown in Figure 7. The red color refers to a positive twist in the core, which is rising in time from 50 hr onward. Note that until 45 hr, the FR is forming, so a weaker twist (less intense red) is realized.

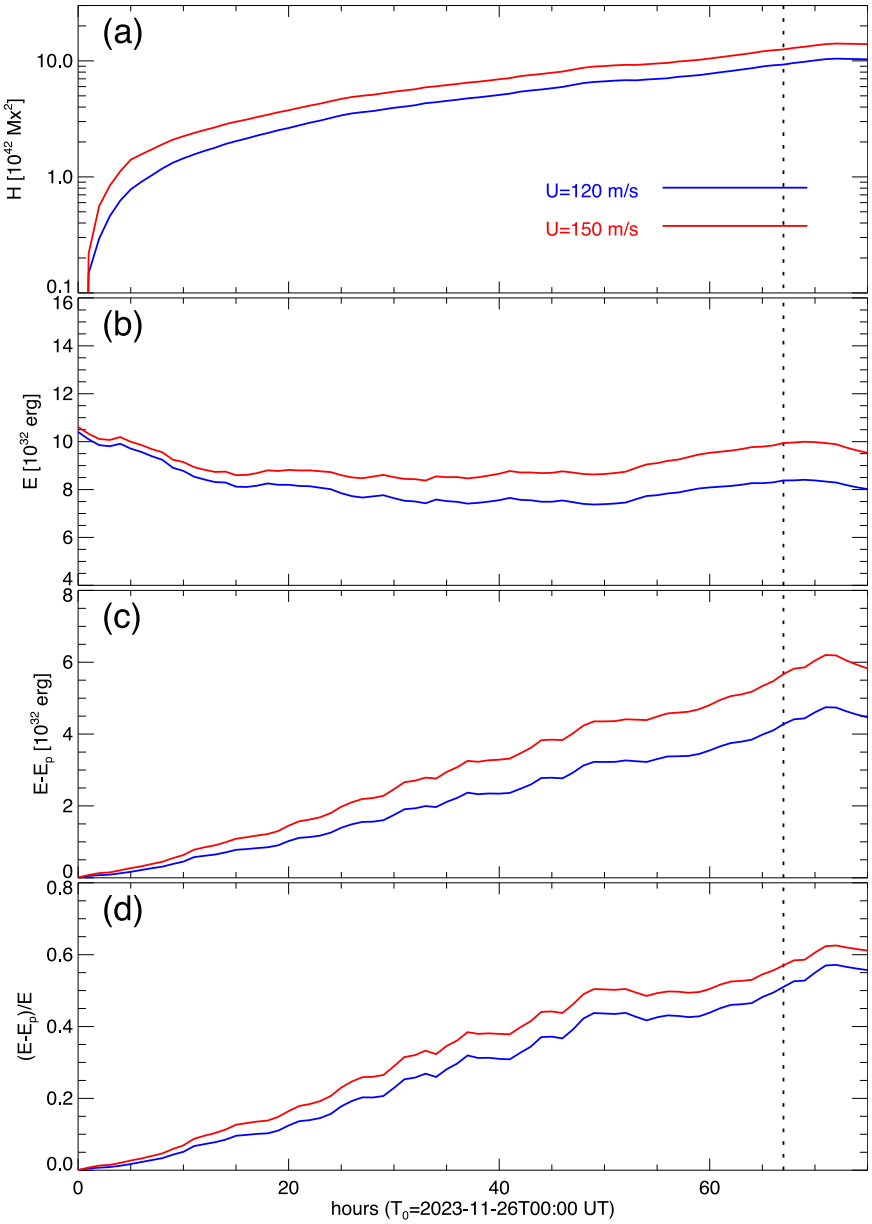

Figure 9. Time evolution of energy and helicity parameters in the computation volume. (a) Total magnetic helicity. (b) Total magnetic energy. (c) Free magnetic energy. (d) Fractional free energy with respect to the total energy. The red and blue correspond to the runs with $U = 120$ m s^{-1} and $U = 150$ m s^{-1}, respectively. The vertical dotted line refers to the eruption time at 19:00 UT on 2023 March 28, at which time the free-energy fraction is 0.51, 0.57.

in our simulations, as MF models are inherently limited by the imposed frictional coefficient.

To support this eruption scenario with the determined helicity ratio, we assess the torus criterion $n = -\frac{z}{B_h}\frac{\partial B_h}{\partial z}$, where $B_h = \sqrt{B_x^2 + B_y^2}$ is the horizontal field strength as a function of height z. Figure 11 presents the decay index n of the simulated magnetic field at 55 hr (blue), 60 hr (green), and 67 hr (red). At these times, n exceeds 1.5 at heights of 29 Mm, 30.5 Mm, and 33.5 Mm, respectively. This behavior indicates a rapidly decreasing overlying magnetic field, while the critical height increases as the FR gradually rises. However, at 67 hr—evident from Figure 7—the FR core (outlined by the yellow oval) has its center located above 30 Mm and its top near 45 Mm. Therefore, the observed eruption time (67 hr) is more appropriate for associating the torus instability with the corresponding H_J/H_V ratio. This observational result further suggests that once the torus instability criterion is satisfied, the helicity ratio (0.3) at the time of the observed eruption may represent an upper limit for triggering the FR eruption. Moreover, in the case of capturing the transition from a slow quasi-static to a fast rise motion, the eruption time is more accurately determined as a reliable basis for comparing H_J/H_V with the critical decay index $n_{\rm crit}$. By self-consistently modeling the AR magnetic field evolution, this study strengthens the evidence for an association between the torus instability and the threshold ratio, while highlighting the need for further case studies to establish its general validity.

4. Summary and Discussion

We have investigated the magnetic origin of the CME that occurred on 2023 November 28 at 19:50 UT from AR 13500 located near the solar disk center. This event was accompanied

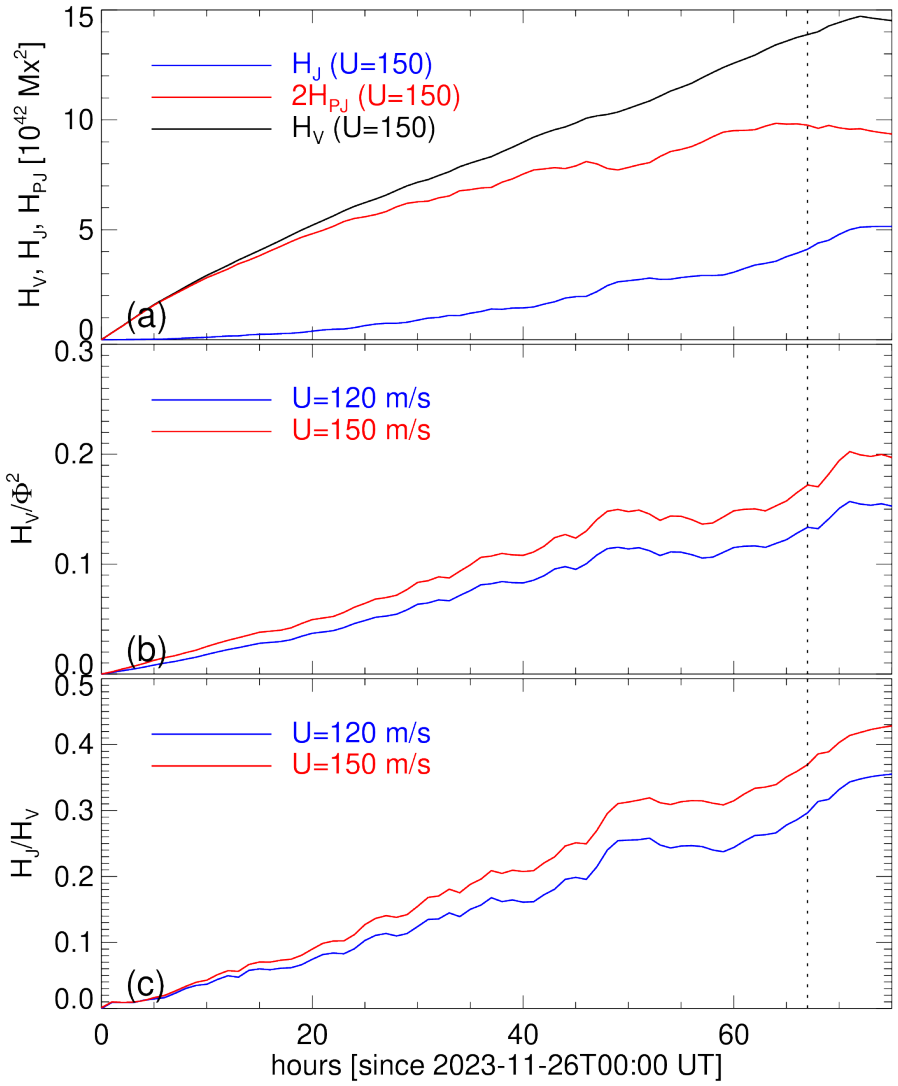

Figure 10. (a) Time evolutions of H_V, H_J, and H_{PJ} for the $U = 150$ m s^{-1} run, (b) of H_V/Φ^2, and (c) of the ratio H_J/H_V for the runs with $U = 120$ and 150 m s^{-1}. The vertical dotted line corresponds to the CME onset time, where the ratio H_J/H_V is 0.3 and 0.37, respectively, for the two runs.

by an M9.8 flare and launched a CME toward Earth at a linear speed of 741 km s^{-1}, whose encounter with Earth triggered an intense geomagnetic storm (-105 nT) on 2023 December 1. The CME was associated with an S-shaped sigmoidal structure supported by inner polarity regions (N2 and P2) forming the main sheared PIL through persistent shear motions, while the outer polarities (N1 and P1) evolved via proper motion (see Figure 2). Over the 3 days of the AR magnetic evolution (2023 November 26–28), the polarities shrank, leading to a decline in the net magnetic flux, while the flux motions injected significant magnetic helicity and energy into the coronal field, accompanied by increasing electric currents and an increasing force-free twist parameter (α_{av}). Notably, the helicity flux peaked at 18:00 UT on 2023 November 28, coinciding with the CME onset at 28T19:50 UT, implying the key role of helicity injection in triggering eruptions. By this time, the AR had accumulated a net helicity of 5×10^{42} Mx^2 and a normalized helicity twist (H/Φ^2) of 0.04 turns, which is above the threshold for confined-flare ARs ($\leqslant$0.02 turns) but below the levels in highly eruptive cases ($\approx$0.15 turns), suggesting a moderate-to-strong eruptive potential of the AR (P. Vemareddy 2017).

By employing the data-driven MF model, we simulate the magnetic evolution of the AR since 2.8 days in advance of the CME eruption. The energy injection for the simulation is controlled by an ad hoc parameter—that is, $U = 150$ m s^{-1} best matches the observed energy injection—yielding a total magnetic energy of 4×10^{32} erg by the eruption time. From the initial PF configuration, the AR evolves gradually into a sheared arcade and further as a twisted FR, mimicking a sigmoid configuration. The proxy emission maps exhibit a strong morphological agreement between simulated and observed sigmoidal features, which is an indication of the right amount of twist in the coronal magnetic field. The FR structure rises slowly from the point of its formation and reaches a height of 80 Mm by the time of its eventual eruption ($T = 67$ hr). In addition, the average field-line twist in the core of the twisted FR reached 1.43 turns, suggesting its critical state for ideal kink instability (T. Török et al. 2004). This FR core twist probably initiated the slow-rise motion to a height of

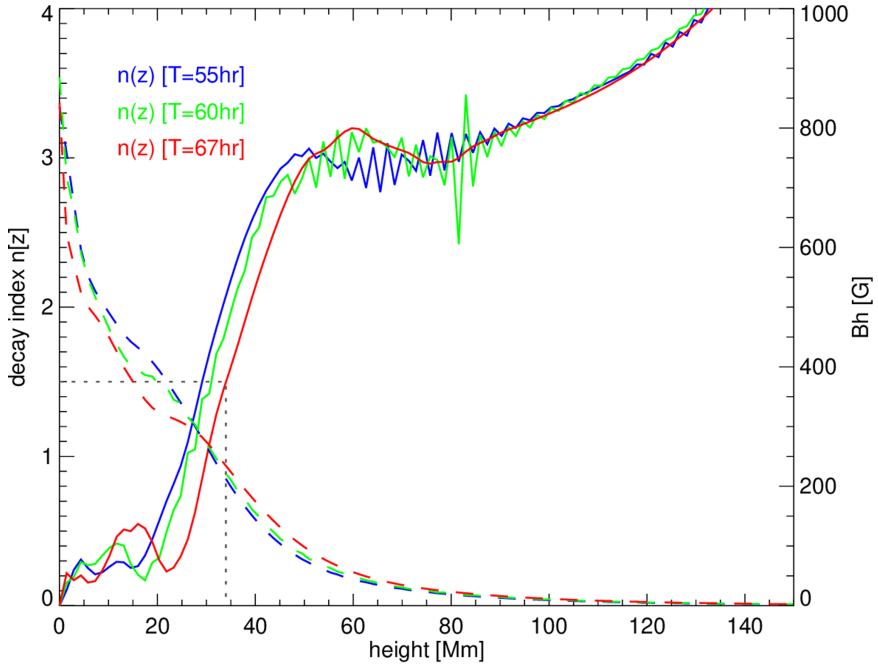

Figure 11. Decay index of the simulated magnetic field at 55 hr (blue), 60 hr (green), and 67 hr (red). The horizontal magnetic field is also plotted with the y-axis on the right. The vertical dotted line corresponds to $n = 1.5$ at 34 ± 1 Mm.

the torus stability domain, as evidenced in the simulated field at 67 hr.

The eruptive behavior of the simulated magnetic field is further evaluated using several nonpotential parameters. Over the 3 days evolution, the relative magnetic helicity (H_V) steadily increases, reaching 14×10^{42} Mx^2, while the free magnetic energy (E_f) rises to 4×10^{32} erg, even as the total magnetic energy (E) slightly decreases due to the decay of the AR. The fractional free energy reaches 57% for $U = 150$ m s^{-1}, indicating the stronger eruptive potential of the AR. The volume of relative helicity is decomposed into a current-carrying component (H_J) and a mutual component between the current-carrying and PFs (H_{PJ}), both of which increase steadily during the formation and further buildup of the FR. Notably, the ratio H_J/H_V attains a value of 0.13 at the time of FR formation ($\approx$50 hr) and exceeds 0.3 by the eruption time (67 hr). These values are aligned with earlier observational and simulation results (E. Pariat et al. 2017; F. P. Zuccarello et al. 2018), suggesting that while $H_J/H_V \geqslant 0.1$ signifies an eruptive tendency, a ratio of $H_J/H_V \geqslant 0.3$ is suggested to be linked with an FR system that is prone to undergoing torus instability and complete eruption. Indeed, the simulated FR core lies well above the torus instability domain at the time of eruption, suggesting an association between torus instability and the threshold helicity ratio, though further case studies are needed to strengthen this relationship.

The data-driven MF simulations reproduce the magnetic field evolution of the AR, accurately capturing key observed features, including the timing of the FR formation and its topology. As these simulations are fully constrained by the observational data, the modeled evolution is considered to closely represent the actual solar conditions, making them a valuable tool for evaluating nonpotential diagnostic parameters across different types of ARs.

Acknowledgments

SDO is a mission of NASA's Living With a Star Program. The field-line rendering was done with the VAPOR visualization software (www.vapor.ucar.edu/). The MF simulations are carried out using the versatile multiuser PENCIL code, which is publicly available at https://pencil-code.nordita.org/. Hα images are obtained from the Hα telescope at Kodaikanal Solar Observatory. We are grateful to the anonymous reviewer for constructive comments that enhanced the objectivity of this work.

ORCID iDs

P. Vemareddy https://orcid.org/0000-0003-4433-8823
S. Nair https://orcid.org/0009-0008-6709-6648
S. Gosain https://orcid.org/0000-0002-5504-6773

References

Aly, J. J. 1990, CoPhC, 59, 13
Ambastha, A., Hagyard, M. J., & West, E. A. 1993, SoPh, 148, 277
Berger, M. A. 2003, in Advances in Nonlinear Dynamics, ed. A. Ferriz-Mas & M. Núñez (CRC Press), 345
Berger, M. A., & Field, G. B. 1984, JFM, 147, 133
Berger, M. A., & Prior, C. 2006, JPhA, 39, 8321
Brown, D. S., Nightingale, R. W., Alexander, D., et al. 2003, SoPh, 216, 79
Chen, P. F., & Shibata, K. 2000, ApJ, 545, 524
Cheung, M. C. M., & DeRosa, M. L. 2012, ApJ, 757, 147
Chintzoglou, G., Zhang, J., Cheung, M. C. M., & Kazachenko, M. 2019, ApJ, 871, 67
Démoulin, P., Mandrini, C. H., Van Driel-Gesztelyi, L., et al. 2002, SoPh, 207, 87
Fisher, G. H., Welsch, B. T., Abbett, W. P., & Bercik, D. J. 2010, ApJ, 715, 242
Forbes, T. G. 2000, JGR, 105, 23153
Green, L. M., Thalmann, J. K., Valori, G., et al. 2022, ApJ, 937, 59
Green, L. M., Török, T., Vršnak, B., Manchester, W., & Veronig, A. 2018, SSRv, 214, 46
Gupta, M., Thalmann, J. K., & Veronig, A. M. 2021, A&A, 653, A69

Leka, K. D., Canfield, R. C., McClymont, A. N., & van Driel-Gesztelyi, L. 1996, ApJ, 462, 547
Lemen, J. R., Title, A. M., Akin, D. J., et al. 2012, SoPh, 275, 17
Liu, R., Kliem, B., Titov, V. S., et al. 2016, ApJ, 818, 148
Pariat, E., Leake, J. E., Valori, G., et al. 2017, A&A, 601, A125
Patsourakos, S., Vourlidas, A., Török, T., et al. 2020, SSRv, 216, 131
Pomoell, J., Lumme, E., & Kilpua, E. 2019, SoPh, 294, 41
Schou, J., Scherrer, P. H., Bush, R. I., et al. 2012, SoPh, 275, 229
Schrijver, C. J., DeRosa, M. L., Metcalf, T., et al. 2008, ApJ, 675, 1637
Schuck, P. W. 2008, ApJ, 683, 1134
Sterling, A. C., Chifor, C., Mason, H. E., Moore, R. L., & Young, P. R. 2010, A&A, 521, A49
Temmer, M. 2021, LRSP, 18, 4
Tian, L., & Alexander, D. 2006, SoPh, 233, 29
Török, T., Kliem, B., & Titov, V. S. 2004, A&A, 413, L27
Vasantharaju, N., Vemareddy, P., Ravindra, B., & Doddamani, V. H. 2018, ApJ, 860, 58
Vemareddy, P. 2015, ApJ, 806, 245
Vemareddy, P. 2017, ApJ, 845, 59
Vemareddy, P. 2019, ApJ, 872, 182
Vemareddy, P. 2024, ApJ, 975, 251
Vemareddy, P., Ambastha, A., & Maurya, R. A. 2012a, ApJ, 761, 60
Vemareddy, P., Ambastha, A., Maurya, R. A., et al. 2012b, ApJ, 761, 86
Vemareddy, P., Cheng, X., & Ravindra, B. 2016, ApJ, 829, 24
Vemareddy, P., Démoulin, P., Sasikumar Raja, K., et al. 2022, ApJ, 927, 108
Vemareddy, P., Warnecke, J., & Bourdin, P. A. 2024, RAA, 24, 025007
Vemareddy, P., & Wiegelmann, T. 2014, ApJ, 792, 40
Wiegelmann, T., & Sakurai, T. 2012, LRSP, 9, 5
Yang, W. H., Sturrock, P. A., & Antiochos, S. K. 1986, ApJ, 309, 383
Zhang, H. 1995, A&A, 304, 541
Zhang, J., Cheng, X., & Ding, M.-D. 2012, NatCo, 3, 747
Zhang, J., Temmer, M., Gopalswamy, N., et al. 2021, PEPS, 8, 56
Zuccarello, F. P., Pariat, E., Valori, G., & Linan, L. 2018, ApJ, 863, 41